Article

133,000 Years of Sedimentary Record in a Contourite Drift in the Western Alboran Sea: Sediment Sources and Paleocurrent Reconstruction

Nieves López-González [1,*], **Belén Alonso** [2], **Carmen Juan** [2], **Gemma Ercilla** [2],
Graziella Bozzano [3], **Isabel Cacho** [4], **David Casas** [5], **Desirée Palomino** [1],
Juan-Tomás Vázquez [1], **Ferran Estrada** [2], **Patricia Bárcenas** [1], **Elia d'Acremont** [6],
Christian Gorini [6] **and Bouchta El Moumni** [7]

1   Instituto Español de Oceanografía (IEO), C.O. Málaga, 29640 Fuengirola, Málaga, Spain
2   Instituto de Ciencias del Mar, CSIC, 08003 Barcelona, Spain
3   Servicio de Hidrografía Naval, División Geología y Geofísica Marina, C1270ABV Buenos Aires, Argentina
4   Departamento de Dinámica de la Tierra y del Océano, Facultad de Ciencias de la Tierra, Universidad de Barcelona, 08028 Barcelona, Spain
5   Instituto Geológico y Minero de España (IGME), 28003 Madrid, Spain
6   Sorbonne Universités, UPMC Univ. Paris 06, ISTEP and CNRS, UMR 7193, F-75005 Paris, France
7   Université Abdelmalek Essaadi, FST, Tangier 90 000, Morocco
*   Correspondence: nieves.lopez@ieo.es

check for updates

Abstract: The Djibouti Ville Drift is part of a contourite depositional system located on the southern side of the Djibouti Ville Seamount in the Alboran Sea (Western Mediterranean). The sedimentary record of a core located in the drift deposits has been characterized to achieve the possible sediment sources for the Saharan dust supply and the paleocurrent variability related to Mediterranean intermediate waters for the last 133 kyr. Three end-member grain-size distributions characterize the sediment record transported by the bottom current to address the different aeolian populations, i.e., coarse EM1, silty EM2, and fine EM3. For these particles, the most likely source areas are the Saharan sedimentary basins and deserts, as well as the cratonic basins of the Sahara-Sahel Dust Corridor. The prevalence of these main source areas is shown in the core record, where a noticeable change occurs during the MIS 5 to MIS 4 transition. Some punctual sediment inputs from the seamount have been recognized during sea-level lowstand, but there is no evidence of fluvial supply in the drift deposits. The paleocurrent reconstruction allows the characterizing of the stadial and cold periods by large increases in the mean sortable silt fraction and UP10, which point to an enhanced bottom current strength related to intermediate water masses. Conversely, interglacial periods are characterized by weaker bottom current activity, which is associated with denser deep water masses. These proxies also recorded the intensified Saharan wind transport that occurred during interstadial/stadial transitions. All these results point to the importance of combining sediment source areas with major climatic oscillations and paleocurrent variability in palaeoceanographic sedimentary archives, which may help to develop future climate prediction models.

1. Introduction

Marine sediments are key for paleoenvironmental studies because they contain some unique clues to understand the poorly known mechanisms driving palaeoceanographic and related paleoclimate

changes. Among them, contourites (i.e., sediments deposited or significantly reworked by persistent bottom currents [1,2] and references therein) are considered to be pivotal features to help understand those changes, because their sedimentary records provide elements to deduce the role of bottom water circulation in transporting the sediment coming from the continent and in seafloor shaping. These deposits are usually characterized by high accumulation rates [3] and provide high resolution records for palaeoceanographic and climate (environmental) reconstructions [1,2,4–8]. When low accumulation rates occur, contourite deposits may provide larger temporal records but of lower resolution for bottom current reconstructions. The deep-water flow behaviour is strongly related to the thermohaline circulation that modulates the global climate. Many studies have addressed the deep water paleocurrent variability related to climatic conditions in the western Mediterranean Sea [9–14], but there is very little information about the intermediate water masses response during the last climatic cycle [15,16].

A natural laboratory for reconstructing the past oceanographic, environmental, and climatic changes is the Mediterranean Sea [17], especially the Alboran Sea, a semi-enclosed basin located between the Mediterranean–Atlantic exchange and close to the subtropical high arid zone (north Africa), where sedimentation is dominated by the contourite ubiquity [18] being the airborne material from the world's largest aeolian dust source (i.e., the Sahara–Sahel Dust Corridor [19]), part of its composition. This combination of large and regional phenomena makes the Alboran Sea a key region for global scale processes. There are many records in the Alboran Sea providing detailed information on climate variation up to the last 50 kyr [10,20–28]. However, only a few studies have extended back to the Late Pleistocene (ca. 120,000 years), such as those recorded by the IODP (Integrated Ocean Drilling Program) expeditions [29,30].

The material from the Sahara–Sahel Dust Corridor [19,31] is characterized by different geochemical compositions depending on the dominant source area [19]. The significant supply of aeolian dust from North Africa to the Alboran Sea since the last glacial cycle has been studied in relation to climate oscillations [23,25,28,32], but only in a few occasions has it been studied in relation to sediment sources [25]. Recent studies about the mineralogy of Saharan dust particles indicate the presence of abundant palygorskite and illite, and relatively high carbonate contents, which are well-known northern and north-western Saharan dust indicators [33].

This study is devoted to reconstructing the possible sediment sources of the Saharan dust supply and the paleocurrent variability of the Mediterranean intermediate water masses for the last 133 kyr (i.e., from Late Pleistocene to Holocene) in a contourite drift associated with the Djibouti Ville Seamount (Alboran Sea). The particular interest of this area is that the influence of fluvial supplies is so scarce that almost all the sediments belong to the aeolian dust inputs that are transported, deposited and reworked by the bottom current. Therefore, contourites of the Alboran Sea would represent an excellent example of a sedimentary record to better understand the connection among the aeolian dust transport and deposition with climate and oceanographic conditions that may improve both paleoclimatic and palaeoceanographic models. To achieve this goal, we present a multiparametric record involving hydrological, sedimentological, geochemical, and isotopic data.

Regional Setting and Present Day Oceanography

The Alboran Sea is a partially land-locked, east–west-oriented basin in the westernmost Mediterranean Sea (Figure 1A) between the Spanish and Moroccan margins. The geodynamic evolution and the main structural features of this basin derive from the relative motion between Eurasia and Africa [34], the result of which is a complex seafloor physiography [35]. One of these main features is the Djibouti–Motril Marginal Plateau [36] (Figure 1B), which has been widely explored in terms of its seabed morphology, seismic stratigraphy, and sedimentary architecture [37,38]. This plateau comprises several seamounts, i.e., Avempace, Herradura, Herradura Spur and Djibouti Ville [39], with reliefs ranging from 500 m on the NE flanks to 1000 m on the SW flanks, and an average top at approximately 200 m water depth (mwd). The study of [37] characterizes these seamounts in detail and emphasizes

the presence of associated narrow contourite moats (1–2 km width and 5.5–10 km length) and drifts. The Djibouti Ville Seamount (summit at 230 mwd, Figure 1C) is round in shape and is dominated by an outcropping hardground partly covered by a thin veneer of soft sediment. Narrow contourite moats and different drift morphologies [18,37] surround the seamount. Here, we refer to the Djibouti Ville Drift (DV drift) as a complex feature formed by moat and drift deposits (from approximately 700 to 900 mwd) at the southern side of the seamount that has been classified as confined contourite [37].
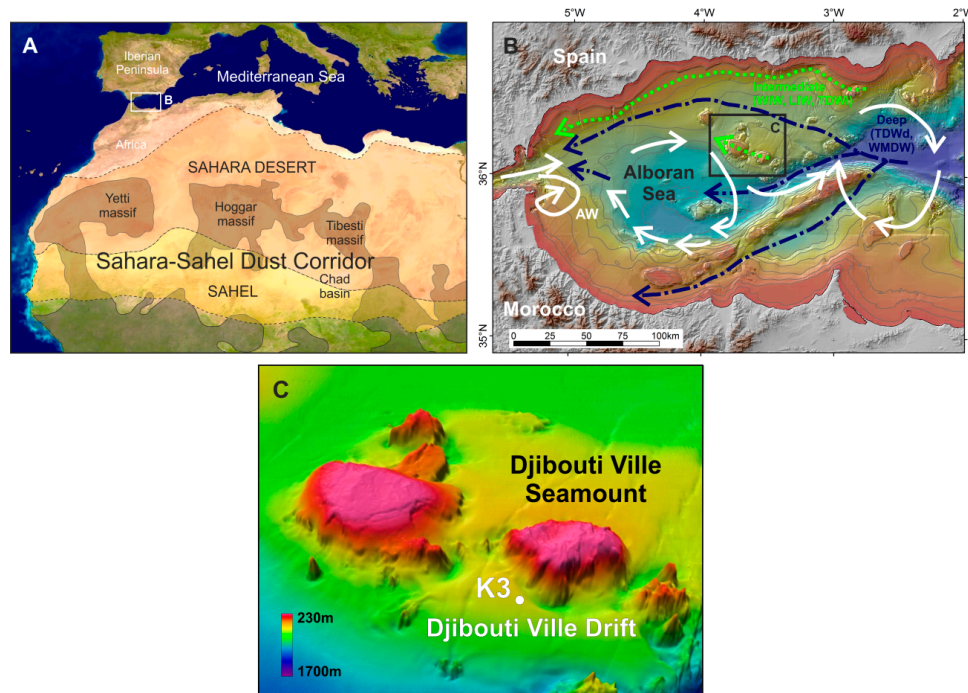

Figure 1. (**A**) Local setting of the study area in the Western Mediterranean Sea and the Sahara–Sahel Dust Corridor. The outcrop of basement rocks is based on [19]. (**B**) Main trajectories of the water masses circulation in the Alboran Sea (based on [18]). Legend: AW, Atlantic Water; WIW, Western Intermediate Water; LIW, Levantine Intermediate Water; TDW, Tyrrhenian Dense Water (i: intermediate, d: deep); WMDW, Western Mediterranean Deep Water. (**C**) 3D bathymetric view of the Djibouti Ville Seamount showing the location of the K3 sediment core at the Djibouti Ville drift.

From an oceanographic point of view, the Alboran Sea is a small sea where Atlantic and Mediterranean waters meet. The Alboran Sea has traditionally been subdivided into the following three major water masses [40,41] (Figure 1B): (i) Modified Atlantic Water (MAW, salinity <36.5–37.5, temperature ~16 °C), which flows eastwards with velocities up to 1 m s^{-1} in a surface layer of 150–250 m; (ii) Levantine Intermediate Water (LIW, high salinity >38.4, temperature ~13.3 °C), which flows westwards with velocities up to 14 cm s^{-1} at an intermediate water depth (200–600 m) and preferentially circulates along the Spanish margin and is formed in the Eastern Mediterranean; and (iii) Western Mediterranean Deep Water (WMDW, salinity ~38.4 and temperature ~12.8 °C), which flows below and moves in pulses with velocities up to 22 cm s^{-1}, is mainly restricted to the Moroccan margin and basins [42,43] and is formed in the Gulf of Lion [41]. Recent studies in the Alboran Sea [44,45] identified surface waters of Atlantic origin (AW) and four water masses with Mediterranean origins (Western Intermediate Water (WIW), LIW, Tyrrhenian Dense Water (TDW), and WMDW). The WIW appears as eddies of colder water flowing above the LIW and is often detached from the coast; the TDW is poorly defined in the Alboran Sea [18] as it shows similar characteristics to the overlying LIW and the underlying WMDW, depending on the year [45] and flows jointly.

In this setting, the Sahara and northern North Africa or Sahel regions are the most likely areas providing dust particles to the Mediterranean Sea [25,31]. Specifically, the so-called Sahara–Sahel Dust Corridor (Figure 1A) is considered the largest aeolian source for dust supply worldwide ([19,46] and

references therein). According to [19], there are four main geological sources for the aeolian dust in this zone: The Precambrian-Paleozoic igneous and metamorphic cratonic rocks, the Mauritania-Chad siliciclastic basins, the Mesozoic-Cenozoic limestones and the marls of the Western Sahara Atlantic margin, and the southernmost ancient basement of the Sahara.

2. Materials and Methods

2.1. Dataset

We have used a selected area of the bathymetric compilation integrated in the regional study of [18]. The dataset of CTD (Conductivity, Temperature and Depth) profiles from 1975 to the present day were downloaded from the Sea Data Net website (http://www.seadatanet.org) and other platforms (e.g., the Medocean II database, http://odv.awi.de/en/data/ocean/medatlasii/); additionally, one CTD obtained during the MONTERA cruise was used to characterize the different water masses in the study area. The sedimentological study is based on the piston core K3 (452 cm recovery) that was retrieved at a water depth of 712 m in the south-central area of the Djibouti Ville Seamount (Figure 1C) during the SAGAS-BIS expedition. This core was located in the southern confined drift deposit under the present-day path of the LIW. After describing the main sedimentary facies and structure, different analyses were performed on the core, as detailed in the coming subsections.

2.2. CTD Analysis

The CTD records were used to elaborate a topographic–hydrographic intersection of the DV drift with the present day water masses. The water masses within the Alboran Sea were defined using the Ocean Data View (ODV) software (http://odv.awi.de), considering the available temperature, salinity, and vertical and horizontal gradient data [40,42,44].

2.3. Chronostratigraphy Analysis

The age model for core K3 was based on the stable oxygen isotope curve and three valid radiocarbon dates (Table 1) for the more recent part of the record (<29.8 kyr). Two additional dating analysis performed on older samples resulted beyond the radiocarbon dating method and they were discarded. This model was correlated to the isotopic record of Site 977 in the Alboran Sea [30]. The stable oxygen isotopes (δ^{18}O) of Globigerina bulloides were measured by a SIRA mass spectrometer [9,20] of the University of Barcelona using approximately 25 specimens picked from up to 300 μm and sampling every 4–5 cm interval. The analytical precision of the laboratory standard was better than ±0.8 for δ^{18}O. The graphical correlation of δ^{18}O was based on the curve proposed by [30] for the Alboran Sea, resulting in an approximately 1.5 kyr sampling resolution. The ^{14}C-ages were determined on monospecific samples (shells of the planktonic foraminifera *Globigerina bulloides*) by Accelerator Mass Spectrometry (AMS) at the Poznan Radiocarbon Laboratory (Poland). To compare our data with other isotopic and paleoclimate records, the radiocarbon dates younger than 29.8 kyr were converted into calendar years (cal yr BP) with the CALIB 7.10 calibration software [47] and the MARINE 13 calibration dataset [48]. The applied local marine reservoir correction (ΔR = −22 ± 35) corresponds to the Málaga site [47]. Table 1 shows the calibrated probability distribution for each age with their respective 1σ confidence range.

Table 1. Coordinates and water depth of the K3 core, radiocarbon accelerator mass spectrometry (AMS) data (*G. bulloides*), and sample age calibration based on the Marine13 curve [48] included in the Calib 7.10 software.

Sagas Core	Latitude (N)	Longitude (W)	Water Depth (m)	Core Depth (cm)	AMS 14-C Age (yr BP)	1σ Calibrated Age (Cal yr BP)	Median Probability Age (Cal yr BP)	Lab Code
K3	36°04.94′	3°35.59′	712	22–23	9950 ± 60	10,842–11,072	10,948	Poz-53720
				49–50	19,760 ± 110	23,148–23,506	23,330	Poz-55671
				87–88	25,320 ± 220	28,729–29,228	28,986	Poz-53721

2.4. Grain Size Analysis

In this study, 107 sediment samples were analysed at 3–8 cm intervals to determine the particle size distribution. Duplicate samples for the bulk and terrigenous fractions were analysed using a Coulter LS 100 laser particle size analyser from the University of Barcelona. This technique determines particle grain sizes between 0.4 and 900 μm as volume percentages (vol.%) based on diffraction laws [49]. The grain size analysis of the terrigenous (carbonate-free) fraction was obtained from previous treatment of the samples with hydrochloric acid (HCl) to remove the carbonate content. To interpret the sedimentary records, the vol% of sand (>63 μm), silt (63–4 μm) and clay (<4 μm), median grain-size (D50) and sorting [50] of both the bulk and terrigenous fractions were calculated using the GRADISTAT package [51]. Similarly, in the terrigenous fraction, we use the silt/clay ratio, the mean grain-size of the sortable silt (SS_{mean}, 10–63 μm particle size range [3,5,52]) and the vol.% of the UP10 fraction (particles >10 μm [13,14,53]) as proxies for the bottom current strength and paleocurrent intensity, respectively.

2.5. End-Member Modelling

An end-member modelling algorithm [54] based on [55] was carried out on the grain size dataset to provide genetically meaningful subpopulations that explain the grain size variance of the system. This technique was applied on the grain-size distribution of the terrigenous fraction (n = 107 samples) of core K3. The minimal number of end members to obtain the best approximation of the variance is determined by calculating the coefficient of determination (r^2). The value of r^2 represents the proportion of the variance of each grain-size class, which can be reproduced by the approximated data [55].

2.6. Sediment Composition Analysis and Statistical Calculations

To characterize and to interpret the environmental changes and source variation, several analytical and statistical techniques were carried out on the core sediments. The magnetic susceptibility (MS), expressed in 10^{-5} SI., was measured every 1 cm resolution on the whole-open section using the GEOTEK Multi-Sensor Core Logger (MSCL) at the Institute of Marine Sciences-CSIC of Barcelona. In the same laboratory, the carbonate content was analysed at a 4–7 cm sampling interval using a Bernard Calcimeter. The elements Al, Si, K, Ti, Fe, Zr, Rb, Sr, Y, and Ca were measured on split sediment core sections at a 1 cm interval resolution by an Avaatech X-ray fluorescence (XRF) core scanner of the University of Barcelona. Each individual power spectrum was transformed by a computer-assisted deconvolution process into the relative contents expressed in counts per seconds (cps). Hierarchical Cluster Analysis (HCA) was carried out to determine the associations among the chemical elements based on their similarities. The obtained dendrogram was based on a single linkage of the Euclidean distance. As XRF analysis provides semi-quantitative content [56], the elemental ratios Ti/Ca and K/Ti have been selected rather than direct counts to recognize the vertical variation. For interpretation purposes, 5-point average curves have been superimposed over those corresponding to measured data ratios.

3. Results

3.1. CTD Records

The temperature and salinity variations along the water column in the intersection zone with the Djibouti Ville Seamount (DVS) allow the characterization of the locations of all the water masses (Figure 2) based on the comparison of our results with the physical characteristics of known Alboran water masses [18,40,44]. The surficial AW displays an almost constant salinity (S) of <36–36.5 psu and an average temperature (T) of 16 °C. The interface with the water mass underneath can be identified in the T–S diagrams by a drop in T, as the WIW has a temperature of 12.9–13 °C and a salinity of 37–37.7 psu. Below the WIW, the LIW is identified by an increase in salinity that reaches 38.5 psu and a temperature of 13.1–13.2 °C. The TDW does not have a large temperature or salinity peak that

allows it to stand out; therefore, it is identified based on its known physical properties (density >29.075 kg·m^{-3}, temperature over 12.85 °C) [44,45]. The WMDW exhibits a lower temperature (<12.7–12 °C) and salinity (38.40–38.52 psu). The topographic–hydrographic intersection of the DVS with the water masses can be observed in Figure 2. Note that the present-day general circulation shows that the upper part of the drift system (<800 mwd), where the sediment core was retrieved (712 mwd), is swept by the LIW and the TDW, while the lower part of the drift system (800 to ca. 1500 mwd) is presently in the path of the WMDW.
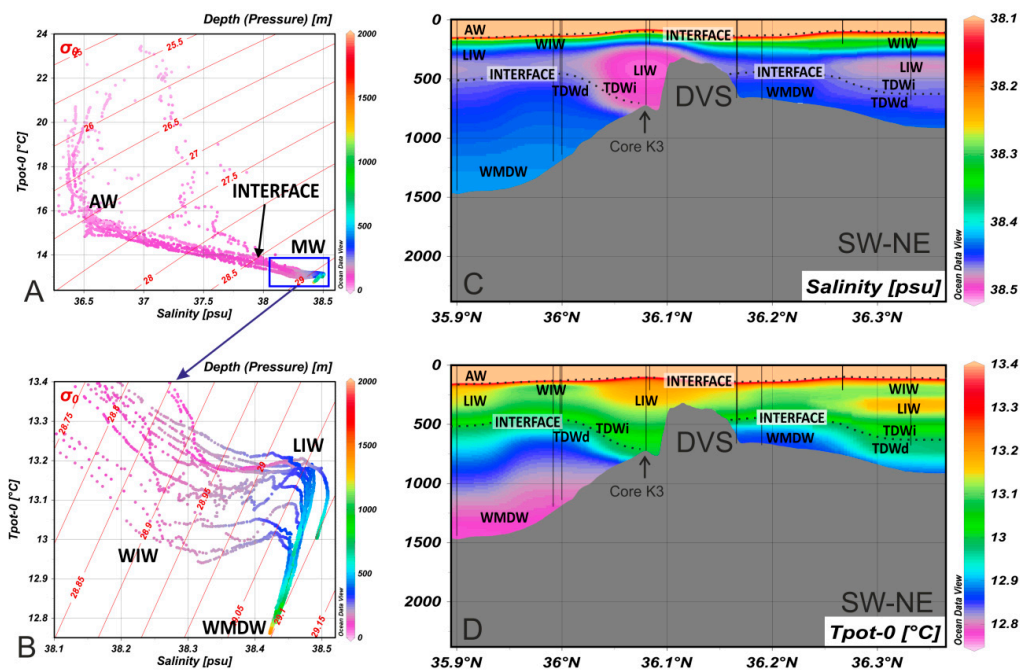

Figure 2. (**A**,**B**) Temperature–Salinity (T–S) diagrams for the major water masses (see Figure 1 for the water masses acronyms) in the study area (Tpot-0, potential temperature θ). Vertical profiles of the (**C**) salinity and (**D**) temperature around the Djibouti Ville Seamount (DVS) area (black vertical lines in the water column indicate the CTD (Conductivity, Temperature and Depth) deployed).

The LIW and the upper part of the TDW (with a composition similar to that of the LIW and, thus, behaving as an intermediate water, i.e., TDWi) are characterized by a significant active circulation [44,45]. On the contrary, the WMDW and the lower part of the TDW (acting as a deep water, i.e., TDWd, with a behaviour similar to that of the WMDW) are characterized by a sluggish circulation before being lifted up into the vicinity of the Strait of Gibraltar [44,45]. In practical terms, the TDW is acting as the interface between intermediate and deep Mediterranean water masses [45].

3.2. Chronostratigraphic Framework and Sedimentation Rate

The age model for core K3 implies an age of 133 kyr at the bottom of the record (451 cm) after δ^{18}O correlation with the chronostratigraphic framework established for the Alboran Sea at Site 977 [30]. This correlation allows the recognition of Marine Isotope Stages (MIS) from MIS 6 to MIS 1 (Figure 3), i.e., glacial (MIS 6, MIS 4, MIS 3, and MIS 2) and interglacial (5e, MIS 1) stages, as well as stadials (5d and 5b) and interstadials (5e, 5c, and 5a). The record of δ^{18}O varies from heavy values of 3.71‰ during the last glacial (MIS 4) to light values of approximately −0.069‰ (interstadial 5e) and 0.87‰ during MIS 1. The most significant depletions of the oxygen isotope occur at both Termination I and II, i.e., the end of MIS 2 and 6, respectively, while the most significant enrichment is observed in the transition from MIS 5 to 4. Millennial-scale variability is also recognized during MIS 3 and 2 by decreases in the δ^{18}O record, which have been indicated as Heinrich Stadials (HS) and Younger Dryas (YD) according to the time intervals proposed for the Alboran Sea [20,57].
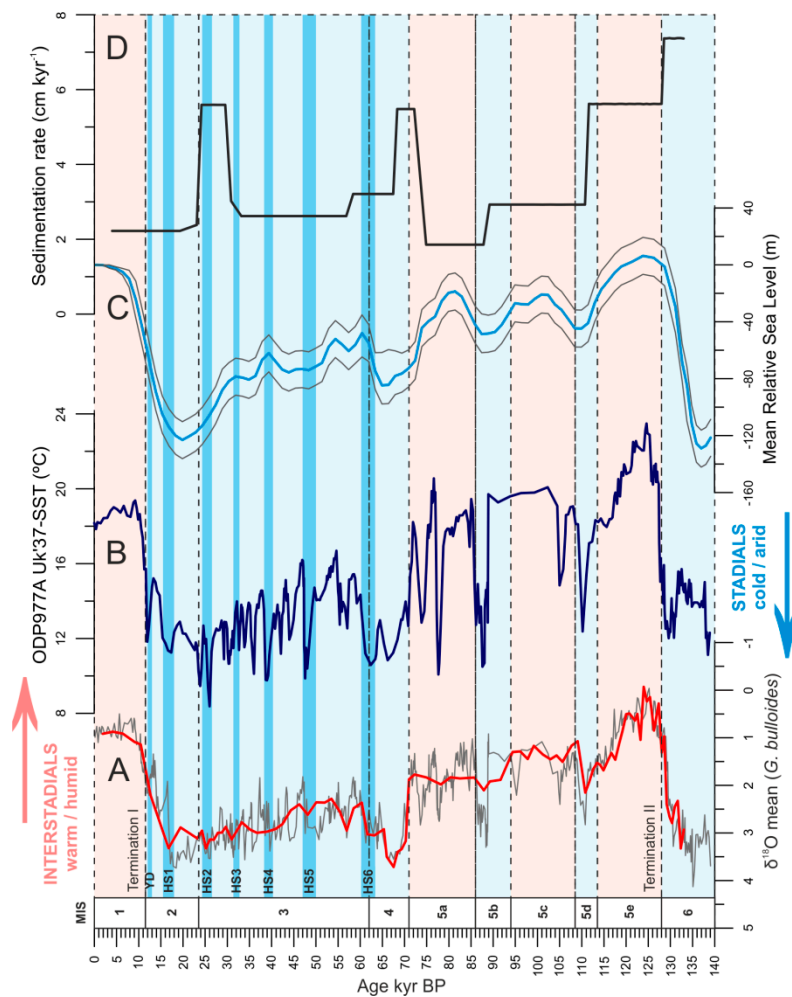
Figure 3. Age model and paleoenvironmental record for the last 140 kyr BP in the Alboran Sea. (**A**) $\delta^{18}O$ of *Globigerina bulloides* in core K3 (red line) compared with the ODP-9774 standard isotope curve (grey line) [30] (plotted with reverse Y axis). (**B**) Sea surface temperatures (SST) of the ODP-977A site based on the measurements of the relative composition of unsaturated C_{37} alkenones [30]. (**C**) Mean Relative Sea Level (RSL) [58]. (**D**) Sedimentation rate calculated for core K3. Marine Isotope Stages (MIS) are indicated by the numbers over the time scale (kyr BP). The stadials (MIS 6, 5d, 5b, 4, 3, and 2) are indicated in clear blue and the interstadials (MIS 5e, 5c, 5a, and 1) in light orange [30]. The Heinrich Stadials (HS 6 to 1, [57]) and Younger Dryas (YD, [20]) are indicated in blue.

The sedimentation rate (SR) of core K3 is remarkably low (<7.3 cm·kyr^{-1}) compared to those estimated in other areas of the Alboran Sea (25 cm kyr^{-1} for the last 20 kyr, [59]; 16.6 and 37.4 cm·kyr^{-1} for the last 25 kyr, [60]). The vertical distribution of the average SR plotted versus the age model of core K3 (Figure 3) exhibit the highest value during MIS 6 (~7.3 cm·kyr^{-1}), followed by stadial 5e (~5.6 cm·kyr^{-1}) and MIS 4 (~5.4 cm·kyr^{-1}). Conversely, the lower values of SR are observed during interstadial 5a (1.8 cm kyr^{-1}) and MIS 1 (2.2 cm·kyr^{-1}). The resulting average SR for core K3 is 4 cm kyr^{-1}.

3.3. Sedimentary Facies and Sequences

The following two main facies can be distinguished based on the texture, grain-size parameters, carbonate content, composition of the sand fraction, sedimentary structures, and vertical succession of the grain-size (Figure 4): (i) Homogeneous mud, and ii) mottled mud to mottled silt and sandy silt facies.
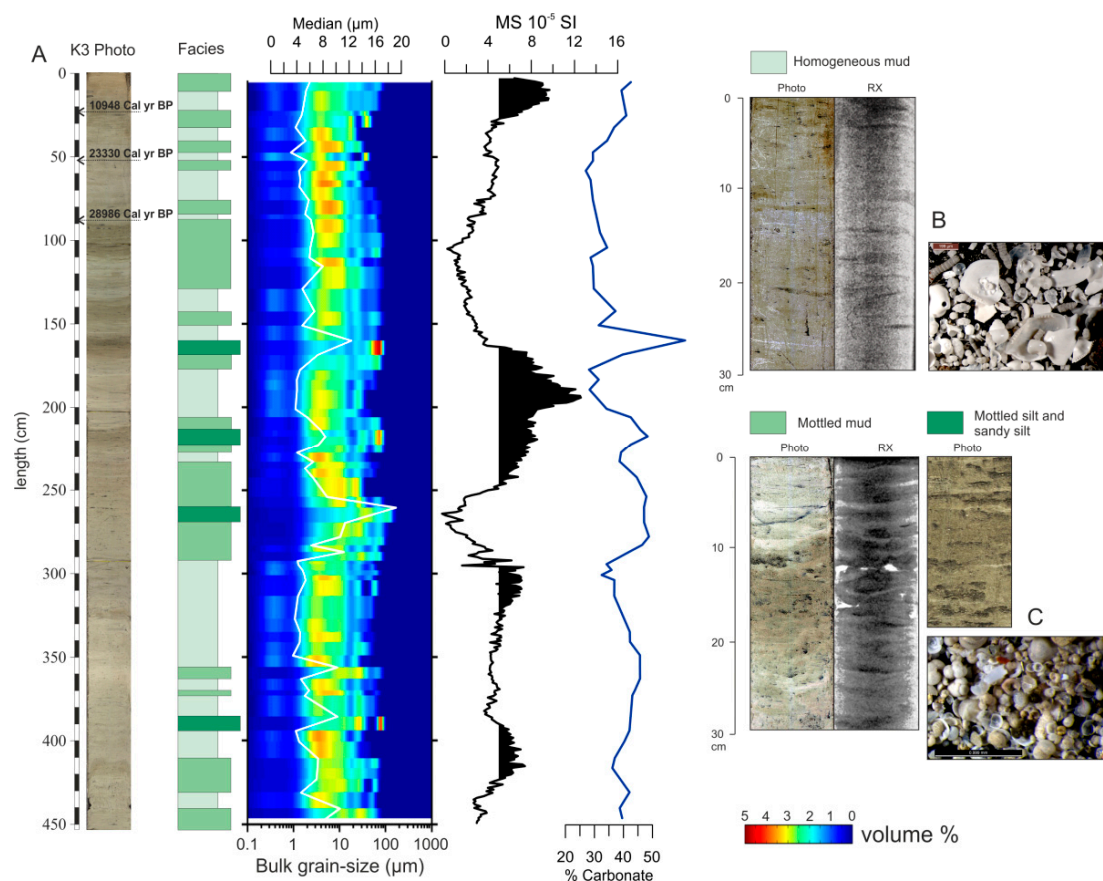
Figure 4. Main sediment core features to characterize the major facies. (**A**) K3 core photo (XRF core scanner) indicating the AMS ^{14}C samples; core log with the sedimentary facies; grain-size distribution (vol.%) and median (µm) of the bulk sediment samples; magnetic susceptibility (MS 10^{-5} SI), where the significant zones are shaded in black; and the carbonate content (weight %). Selected pictures of the original sediment (digitally treated), the corresponding radiography and the binocular microscope photo of the main components observed in the homogeneous mud facies (**B**) and in the mottled mud to mottled silt and sandy silt facies (**C**).

The homogeneous mud facies (Figure 4B) is the finest-grained, with >40% clay. It is a very poorly sorted (3–5 µm) silty clay with a median grain size less than 5 µm. The carbonate content is relatively high (27–46 weight %). The sand-sized material is predominantly planktonic and benthic foraminifera shells (individuals and fragments) and fragments of bivalves and ostracods. This facies looks very monotonous, although indistinct and discontinuous parallel lamination and some mottles and small lenses are sometimes visible. When bioturbation is observed, it grades from low to moderate and is often marked by thin filaments of iron sulphides. This facies appears in intervals from a few centimetres (<10 cm) to almost 80 cm.

The mottled mud to mottled silt and sandy silt facies (Figure 4C) can be subdivided into two subfacies with respect to the relative proportions of sand, silt, and clay. Thus, it is predominantly mottled mud when containing lenses of silt and a median grain size between 5 and 11 µm, while it is mottled silt and sandy silt when containing lenses of mud with a median grain size ranging from 8 to 19 µm. In both cases, they are very poorly sorted (3–5 µm). In general, the carbonate content varies between 29 and 49 weight %, although the subfacies of mottled silt and sandy silt is more enriched, containing one sample that reached up to 61%. The sand-sized material is predominantly (90%) foraminifera shells (individuals and fragments) and shell debris (mainly bivalves). This facies is clearly distinguished visually since it comprises either a rapid alternation of thin irregular mud or silt layers or, commonly, a completely irregular arrangement of these sediment types in pockets and lenses.

The vertical succession of these facies allows the definition of sequences characterized by coarsening-up and fining-up grain size distributions as bi-gradational patterns. Thus, two zones of the sediment record display a complete sequence of the facies defining, from the base to the top, by homogeneous mud, mottled mud, mottled silt and sandy silt, and then the same facies in a reverse mode, i.e., mottled mud and homogeneous mud. These two zones are from ca. 310 to 230 cm and from 230 to 190 cm. Other truncated bi-gradational sequences imply a partial succession of these facies starting with homogenous mud, mottled mud, mottled silt and sandy silt and again homogeneous mud (from ca. 190 to 150 cm). The less complete sequences are represented by only the fine homogenous mud and the coarser mottled mud (mainly at the base of the core and in the top 150 cm), or the homogeneous mud and mottled silt and sandy silt (at approximately 380–400 cm).

3.4. End-Member Modelling and Grain-Size Parameters

To help understanding the variations in paleocurrent intensity and the most likely sediment sources for the last 133 kyr in the DV drift, an end-member modelling algorithm and a set of grain size parameters (clay content, UP10, mean grain-size of the sortable silt fraction, and silt/clay ratio) have been calculated on the terrigenous sediment fraction.

The end-member modelling of the grain-size distributions have allowed the recognition of three main end-members (EM), of which the characteristics are shown in Figure 5. The goodness of fit for this approximation displays a mean coefficient of determination (r^2) of 0.93 and explains the grain-size spectrum from ca. 0.25 to 65 µm for a coefficient of determination of >0.5. EM1 is the coarsest, with a median grain size of 36 µm and 31% sand and 58% silt (11% clay). EM2 is mainly silty (63%), with a minor content of clay (23%) and sand (14%) and a median grain size of 9 µm. EM3 is the finest (3 µm median grain size), with 63% clay and 24% silt (13% sand). EM1 and EM2 are almost unimodal, with principal modal sizes of 47 µm (coarse silt) and 12 µm (fine silt), respectively. The polymodal EM3 grain-size distribution is mainly characterized by modal sizes of 3 µm (coarse clay) and <1 µm (clay). The secondary modes of these EM are represented by low frequency values that have not been considered in this study, since the model introduces artificial modes in classes where other EMs have their primary modes or where they overlap [54,61]. EM3 is predominant lengthwise the core (37% of the record), while EM1 and EM2 display similar dominance (32% and 31%, respectively) (Figure 6C).
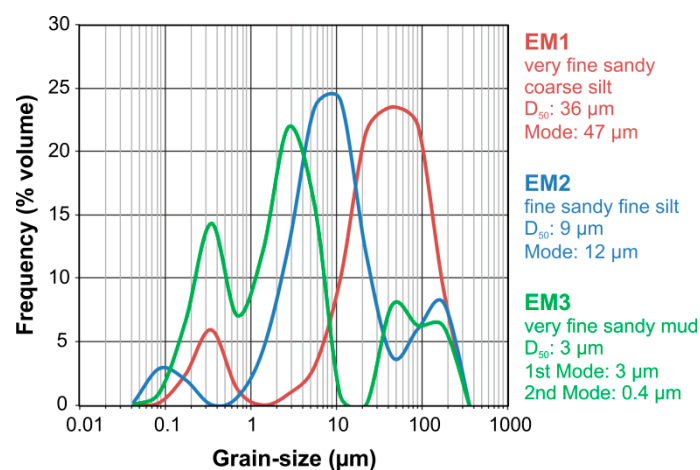

Figure 5. Grain-size distribution after end-member modelling analysis of the sediment samples (n = 107) for core K3. The end-member loadings represent the sedimentologically interpretable unmixed grain-size distributions [54].
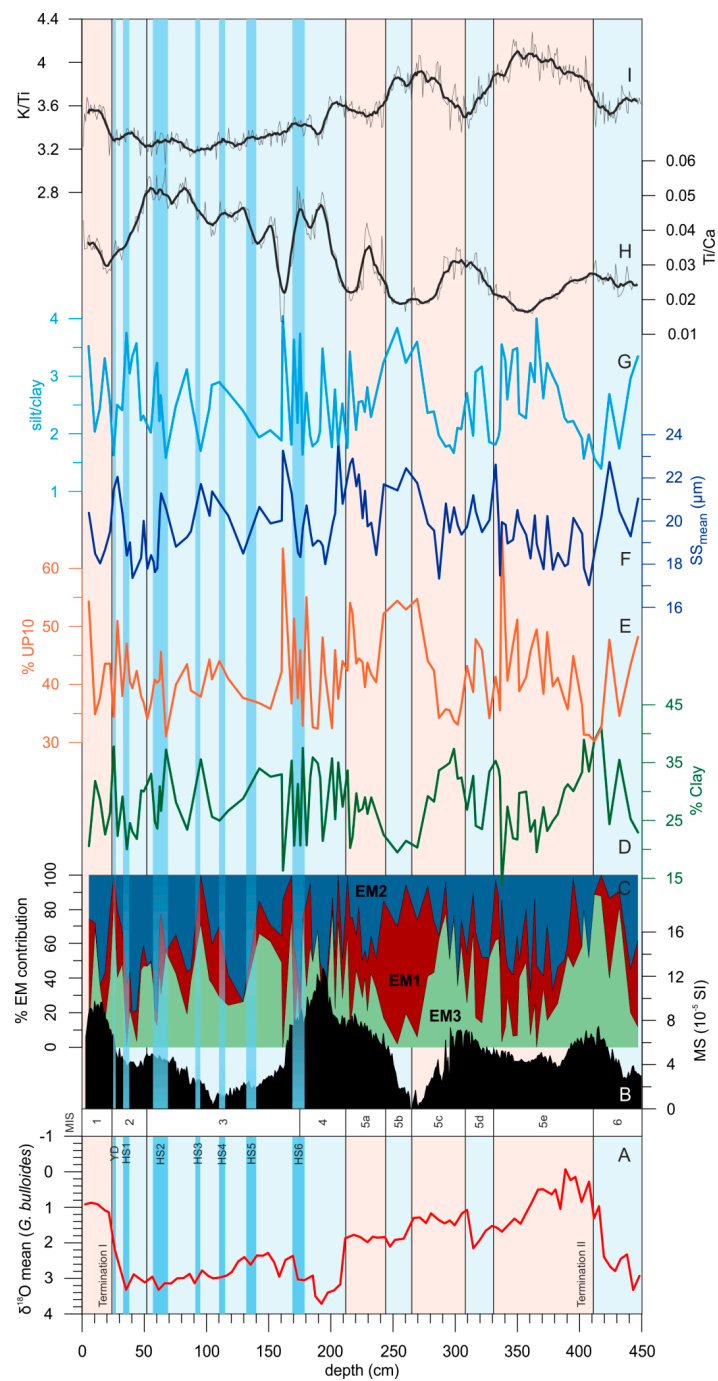
Figure 6. Vertical variation in the grain-size and geochemical parameters in core K3. (**A**) Chronostratigraphic framework based on $\delta^{18}O$ of *Globigerina bulloides* (plotted with reverse Y axis) (see Figure 3 for more details). (**B**) Magnetic susceptibility (MS 10^{-5} SI). (**C**) End-member scores (%contribution) displaying the proportion of variance explained by the 3 end-members for each individual sample. (**D**) Clay content (vol.%). (**E**) UP10 fraction (vol.%) that corresponds to particles >10 µm [13,14]. (**F**) Mean grain-size of the sortable silt fraction (SS$_{mean}$) corresponding to the 10–63 µm particle size range [3]. (**G**) silt/clay ratio. (**H**) Ti/Ca ratio of XRF counts. (**I**) K/Ti ratio of XRF counts. Marine Isotope Stages (MIS) of the stadials (MIS 6, 5d, 5b, 4, 3, and 2) are indicated in clear blue and the interstadials (MIS 5e, 5c, 5a, and 1) are in light orange [30]. The Heinrich Stadials (HS 6 to 1, [57]) and Younger Dryas (YD, [20]) are indicated in dark blue.

From all grain-size textural groups, only the terrigenous clay content (vol.%) has been plotted (Figure 6D). In general, there is a decreasing tendency during the interstadials (MIS 5e, 5c, 5a, and MIS 1). Conversely, in the stadials (end of MIS 6, MIS 5d, and MIS 4 to 2) and before cold periods (HS 6, 5, 3, 2, and YD), higher contents of clay are observed, reaching a maximum value of 41% (MIS 6). As an exception, stadial MIS 5b is characterized by a low clay content, with an average value of 21%. It is worth mentioning that the clay content tendency almost mimics the EM3 contribution lengthwise the core. The values of UP10 clearly show significant variations from MIS 6 to MIS 1 (Figure 6E). General increasing tendencies are observed during the interstadials (MIS 5e, 5c, and 5a), reaching values of up to 54%. However, maximum peaks are observed just before the stadials (MIS 5d and 5b) achieving values up to 67%. In the last glacial period (MIS 4 to MIS 2), the high UP10 values match with some HS cold events (HS 4, 2, and 1), although the most significant peak is reached after HS 6 (63%). The mean grain-size of the sortable silt fraction (SS_{mean}) varies from 17 to 24 μm, with an average value of 20 μm (Figure 6F). There is a clear increasing tendency of SS_{mean} from ca. 17 μm, at the beginning of interstadials (MIS 5e, 5c, and 5a), to ca. 23–24 μm, at the end of these warm periods and in some stadial periods (end of MIS 6, MIS 5b, and MIS 4). The silt/clay ratio (Figure 6G) during stadials and cold periods clearly displays increasing or high values (up to 3.8), while the interstadials are characterized by decreasing or low values (up to 1.7). When comparing the vertical evolution of this ratio with the curve of the mean relative sea level (Figure 3), there is a noticeable coincidence between the high silt/clay ratio values and most of the sea-level lowstands that characterize the stadial periods.

3.5. Magnetic Susceptibility and Sediment Geochemistry

The geochemical composition of the core sediments plays an important role in the magnetic susceptibility values and both are mainly related to the source area of the sediments that fed the DV drift. The magnetic susceptibility (MS) in core K3 ranges from -0.2 to 12.6×10^{-5} SI, with an average value of 4.8×10^{-5} SI (Figure 4A). The more remarkable MS peaks are between 10–16 cm and 189–195 cm, with approximately 9×10^{-5} SI and 12×10^{-5} SI, respectively. There are two other peaks of high MS between $6–7 \times 10^{-5}$ SI at 296–318 cm and at a 398–420 cm core depth. The low MS signal is sometimes related to carbonate dilution, as can be observed at 160 cm and from a core depth between 250 to 270 cm, where an increasing carbonate content is observed.

The possible relationship among the chemical elements analysed in the core K3 sediments (Al, Si, K, Ti, Fe, Zr, Rb, Sr, Y, Ca) has been explored by applying Hierarchical Cluster Analysis (Figure 7). Four main clusters were evidenced through this statistical analysis, which allows the establishment of four main compositional groups of elements. From these clusters, two main lithogenic groups are clearly distinguished, i.e., cluster 1 (C1) that comprises Si and K, and cluster 2 (C2) that includes Sr, Ti, Y, Rb, Al, and Zr. Cluster 3 (C3) only involves Fe as a Fe-bearing group, and cluster 4 (C4) is just characterized by Ca as a carbonate group.

Selected geochemical ratios (Ti/Ca and K/Ti) have been plotted to determine the variation of the sediment composition for the last 133 kyr (Figure 6H,I). The record of Ti/Ca is related to changes in the contribution of siliciclastic Ti-bearing minerals [62] versus biogenic (calcium carbonate from shells) and possibly detrital Ca to the sediments. In core K3, there is a sharp increase in the Ti/Ca record from MIS 5a to MIS 4 (from 0.02 to 0.05, Figure 6H). During MIS 5, this ratio shows decreasing/increasing tendencies, but they are not exactly synchronous with interstadials/stadials. However, during the last glacial period (from MIS 4 to 2), this ratio reaches maximum values (up to 0.06), with the exception of the zone between 160–165 cm core depth because of carbonate dilution (see % carbonate peak in Figure 4A). To differentiate the sediment sources of the detrital fraction [63], the record of the K/Ti ratio has been calculated (Figure 6I). These two elements are associated with silicates, i.e., K is mainly concentrated in potassium feldspars and illite, while Ti is largely present in heavy minerals (e.g., rutile and ilmenite). In core K3, the K/Ti ratio shows a clear general diminishing from Termination II to I (from ca. 4.3 to 3.2). In general, two main behaviours characterize the core record. From the end of MIS 6 to MIS 3, there are increasing and decreasing tendencies that seem to be related to interstadials

and stadials, respectively, with values ranging from 4.3 to 3.4. The stadial period that comprises MIS 3 and MIS2 is characterized by a very flat tendency with an average value of 3.3, although some slight fluctuations can be noticed during MIS 3 where K/Ti minor peaks are coincident with the majority of HS.
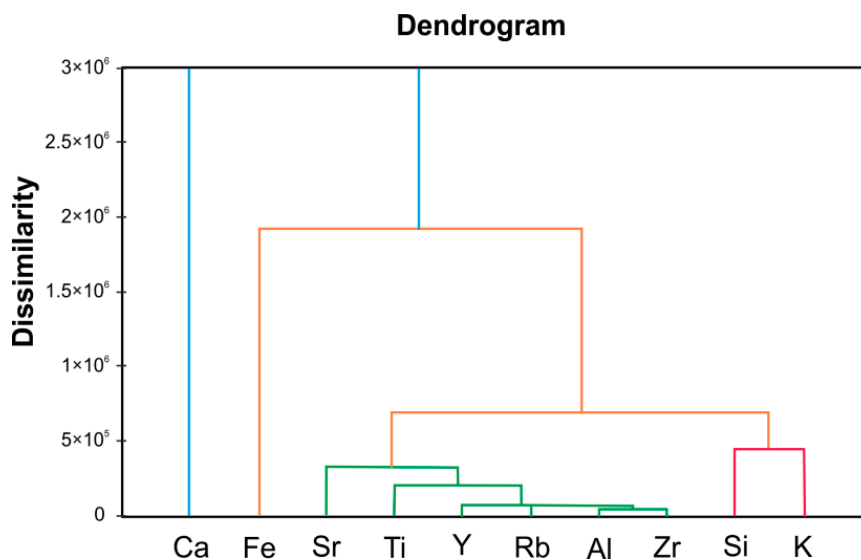

Figure 7. Dendrogram from the Hierarchical Cluster Analysis (HCA) by using the single linkage as agglomeration method of the Euclidean distances.

4. Discussion

4.1. Drift Sediment Sources

The results of the end-member modelling indicate that three main grain-size distributions characterize the DV drift sediments (Figure 5). The coarse EM1 (36 μm median and 47 μm modal sizes) may correspond to the large dust defined by [64] for the North Africa airborne dust. They define these particles as approximately in the 20–60 μm size range (coarse or very coarse silt), which consists of predominantly quartz [65] and other primary minerals, such as various feldspars and perhaps some calcite and dolomite. The large dust travels in suspension, but usually for fairly short distances of 20–100 km, although very large storms can lift large dust particles to great heights and sometimes produce extensive transports. The fine EM3 (3 μm median and modal sizes) matches with the small dust of [64], who defined these particles in the <10 μm (the PM10) range, probably concentrated into the 2–6 μm region (fine or very fine silt and clay). They consist of clay minerals [65] and fine primary mineral particles, typically quartz and feldspar that are carried in high suspension. This bimodality of the dust appears to be a direct result of the early events that control the production of dust particles at the source area instead of the aerial transport [65]. These two dust sizes are separated by a medium silt zone, i.e., 8–16 μm [64], that coincides with the properties of EM2 (9 μm median and 12 μm modal sizes) that would represent the background size transported in average conditions.

The groups of elements defined by the HCA (Figure 7) of the geochemical composition of the drift sediments suggest different source areas, mainly related with the Sahara–Sahel Dust Corridor. The lithogenic group C1 (defined by Si and K) seems to be related with the aeolian dust sourced from the Sahara Sedimentary Basin (SSB) and deserts. These areas are mainly characterized by felsic composition of mostly clay minerals and quartz, and are affected by physical winnowing and chemical breakdown [19]. Recent studies of western Mediterranean marine sediments reveal that clay sediments are dominantly illite (main carrier of K) and kaolinite, with lesser amounts of smectite, chlorite, and palygorskite [25]. The other lithogenic group C2 (Sr, Ti, Y, Rb, Al, and Zr) may be related to the aeolian dust from the igneous and metamorphic terrains of the Saharan Cratonic Basin (SCB). These

particles are rich in more soluble major elements (e.g., Na) and LILE (e.g., Rb, Sr) as well as accessory minerals containing HFSE (e.g., Zr, Hf, Th) and REE [19]. Thus, sediments from the SCB area may contain Zr-rich accessory minerals (zircon), Rb-rich particles related to detrital clay minerals (such as mica [66]), and Ti-bearing minerals (e.g., ilmenite, rutile), which have been successfully used as aeolian proxies [67,68]. Although the Saharan–Sahel Dust Corridor is considered the most important source area, a local provenance for the drift sediments cannot be ruled out. In fact, the Fe-bearing group C3 (Fe) is probably related to the sediments provided by the reworking of the seamount volcanic deposits. Some samples retrieved by dredging in different oceanographic expeditions [69,70] revealed the volcanic nature of the Djibouti Ville Seamount. They were characterized by pieces of volcanic rocks, abundant coral fragments, muddy sediments, and Mn-crusts. Most of the volcanic samples were non vesicular, heavily altered andesites with a greenish granular appearance due to the alteration of former pyroxene and plagioclase phenocrysts to a chlorite rich groundmass [70]. Other possible sources are volcanic rocks of the adjacent seamounts (e.g., Alboran Island, Yusuf Ridge, Al Mansour Seamount) that have been detected at Site 978 [71] and may have been transported by bottom currents. The carbonate group C4 (Ca) may be composed of particles of biogenic and/or detrital origin since the Alboran Sea is characterized by particles of mixed origin [14]. The north-westernmost source area of aeolian dust is the African Atlantic margin (AM), which is mainly enriched in detrital carbonate particles such as carbonates and dolomites [19]. Unfortunately, in this study, we are not able to distinguish between these two origins of the carbonate. Further studies are desirable to fully understand the relationship between the geochemical groups and the mineralogy of the sediments that allow distinguishing the source areas of the aeolian particles deposited in the drift.

The combination of different proxies has allowed the establishment of the most likely source areas for the last 133 kyr in the study area. The K/Ti variation emphasizes differences in the terrigenous particles provenance related to changes in their geochemical composition [66]. The Ti/Ca record is commonly used as a proxy for the dust supply (e.g., [72]), allowing assessment of the continental aridity and relative wind strength. In addition to the geochemical imprint, the grain-size distribution is crucial to infer relative wind strengths since more vigorous winds may transport larger grain sizes from the source area [67]. During MIS 5 interstadials (Figure 6), the most likely source area of the drift sediments is the SSB since these zones are enriched in quartz and illite [73]. This interpretation is supported by the opposite tendencies in Ti/Ca (lowering) and K/Ti (increasing) that are synchronous with the increasing tendencies of UP10 and the silt/clay ratio until the MIS 5–4 transition. This points out to the dominance of relatively coarse Saharan dust composed by K-bearing minerals (e.g., illite, K-feldspars), as suggested by [46]. This may be enhanced by the proximity of the source areas due to more humid and high sea-level conditions, although some fluvial sediment cannot be totally discarded. An important change in the source area for the dust supply during the MIS 4 stadial can be suggested by the decrease in the K/Ti ratio (Figure 6I), which also coincides with an important lowstand of ca. 90 m below the present mean relative sea-level (mean RLS) (Figure 3C). By this time, the core record also shows a very sharp peak in the MS (maximum value of 12.6×10^{-5} SI), Ti/Ca, UP10, silt/clay, and silty EM2. Thus, for MIS 4, the most likely source areas for the drift sediments are both SCB and reworking seamount deposits (Ti- and Fe-bearing sediments). This may be enhanced by bottom currents locally accelerated by the presence of seamounts [74] that are able to accumulate coarser particles in the drift and to promote winnowing processes of fine sediments. During the last glacial period (from MIS 4 to 2), the K/Ti ratio decreased but remains quite constant, while Ti/Ca displays an important increase related to both the higher presence of Ti-bearing minerals and the lower content of Ca-rich particles. During the glacial stages and coinciding with a positive NAO (North Atlantic Oscillation) index, an intensification of the atmospheric circulation and westerly winds favour arid conditions in the Mediterranean and northern Africa [32,75], allowing enhanced Saharan aeolian dust transport to the Alboran Sea [76]. Thus, the observed increasing in Ti-bearing particles may come from the aeolian supply from SCB areas with a contribution of the seamount deposits, due to the RSL decline [58] and enhanced bottom currents. The short record in the Holocene sediments (MIS 1) indicates a return to

the interstadial conditions, mainly characterized by an increase in K/Ti, UP10, and silt/clay together with low values of Ti/Ca.

The sedimentary record of the DV drift suggests that mainly the aeolian supply from the Sahara–Sahel Dust Corridor reaches the study area since no geochemical or sedimentological evidence of fluvial sediment delivery has been recognized. We tentatively suggest that the lack of sediment from fluvial origin could be related to the interplay of the following two facts: (i) The relatively isolated position of the seamount and related drift that are separated from the Spanish proximal continental margin by an intraslope basin and from the Moroccan margin by deep sea basin plains; and ii) the alongslope piracy of the fluvial sediments when arriving to the sea by the Atlantic and Mediterranean waters [77].

4.2. Paleocurrent Reconstruction of the Intermediate and Deep Flows

The bottom currents that sweep the study area are the LIW, the TDW and the WMDW (Figure 2), in which the general circulation remained active during the time frame examined in this study. Thus, the changes in the DV drift composition and formation for the last 133 kyr have been mainly controlled by the sediment influx and bottom current strength. The variability in the bottom current strength can be interpreted in terms of the relative intensity and vertical migration of the water masses affecting the contourite system. This paleocurrent reconstruction will assume (a) the TDW acts as the interface between intermediate and deep water masses [45]; and (b) the intermediate water masses are characterized by a significant circulation, which is opposite to the deep water masses that are characterized by a sluggish circulation [44,45]. Taking these considerations into account, any indicator of a faster flow points to the action of intermediate waters (either as a result of an increase in its general velocity or a deepening of the interface between intermediate and deep waters), and any indicator of a slower flow points to the action of deep waters (mostly a result of a shoaling of the interface).

In addition, it is important to consider that changes of the intermediate water density in response to cooler temperatures [78] and increasing salinities [10] in the Mediterranean Sea during glacial intervals favour the deepening of the LIW core, which would deepen the interface between intermediate and dense deep waters. The study of [15] also demonstrates that the LIW axis fluctuates in-phase with both climate and sea-level changes. These authors associated the alternating deepening/shoaling of the intermediate water mass with a sea-level fall/rise (i.e., vertical translation) and climate degradation/amelioration (i.e., density changes), respectively.

Furthermore, the paleoenvironmental conditions in the source areas also play an important role in the sediment availability. The sedimentary record of core K3 corresponds to fine-grained contourite deposits [2] characterized by bi-gradational sequences of the facies that match with the sediment divisions of [79], denoted as C1 to C5. Thus, two main complete sequences (i.e., C1-C2-C3-C4-C5) are observed from MIS 5c to MIS 5a and from this last to MIS 4, which are related to long-term changes in the bottom-current velocity [2,79]. A partial sequence comprising C1-C2-C3-C5 is observed from MIS 4 to the first 8 kyr of MIS 3. Truncated sequences of C1-C2-C5 and C1-C3-C5 are observed in the rest of the core record.

The offset of glacial MIS 6 (Termination II) is characterized by cold temperatures and heavy $\delta^{18}O$ during relative sea level rise conditions (Figure 3). The short record for the end of MIS 6 shows the effect of strong bottom-currents (i.e., the LIW) inferred from high values of paleocurrent proxies UP10 and SS_{mean} (Figures 6E and 6F, respectively) as well as the important contribution of the coarse EM1. These proxies experience a sharp decay in the transition to MIS 5 at the RSL highstand [58] that match with a minimum in the silt/clay ratio and the silty EM2. All these proxies evidence an important deceleration in the currents and suggest an abrupt change from a cold to a warm period, as is also observed in the Sea Surface Temperature (SST) record for the Alboran Sea [30] (Figure 3). By this time, there is a high SR (7.4 cm·kyr^{-1}), which is mainly associated with an increased clay content (and so EM3) as consequence of sluggish bottom currents and a high aeolian fine dust supply (high MS and relatively high Ti/Ca, Figures 6B and 6H, respectively). The progressive deceleration of the currents

from strong to sluggish points to the shoaling of the LIW core associated with a shallower interface between intermediate and deep waters. As a result, the DV drift transitions from being affected by the LIW to being swept by the WMDW.

The last interglacial MIS 5 is characterized by a significant variability in all paleocurrent proxies, alternating long interstadials (5e, 5c, and 5a) with short stadials (5d and 5b). In general, coarse-grained intervals reflect bottom-current intensification, generating sediment re-suspension of previously deposited material and winnowing of finer particles [4]. This interpretation is supported by the associated increase in the paleocurrent speed proxies (UP10, SS_{mean}) and silt/clay. The onset of MIS 5 (i.e., MIS 5e interstadial) is the warmest interglacial period and coincides with an RSL highstand (Figure 3) of the same magnitude as that of the present day RSL [58]. During this period, the drift sedimentation is dominated by the silty EM2 of K-enriched composition (Figures 6C and 6I, respectively) that probably comes from the SSB source area. These conditions and the high average values of the silt/clay ratio indicate moderate bottom currents transporting and settling homogeneous mud facies with some intercalations of mottled mud. This has also been observed in other areas of the Western Mediterranean [15] where freshwater flooding produces more stable water stratification that inhibit vertical mixing and ventilation of intermediate to deep water masses [80,81]. During these warm and humid conditions [82], only some punctual moments of strong winds are recorded as EM1 peaks (Figure 6C). The higher stratification and inhibition of the vertical mixing indicate a high contrast between the upper and lower TDW. The moderate velocities also suggest the action of a current not as active as the LIW, possibly the TDW. In addition, this would favour the action of internal waves travelling along the interface between intermediate and deep waters (i.e., between the upper and lower TDW) [45]. This is in agreement with the high variability observed in all the paleocurrent proxies.

The short stadial MIS 5d is characterized by a sharp temperature decreasing under moderately heavier $\delta^{18}O$ [30] (Figure 3). The sedimentary record displays relatively high values of UP10 and SS_{mean} (Figures 6E and 6F, respectively), suggesting an enhanced flow-speed of the bottom current coinciding with a high silt/clay ratio and an RSL decrease [58]. At this time, renewed LIW ventilation is observed in both the western [15] and eastern [83] Mediterranean. This lowstand situation already favours the deepening of the interface, also favoured by the cold conditions that would deepen the core of the LIW and thus further deepen the interface. This is supported by the enhanced flow-speed, all pointing to the action of the LIW on the DV drift, which may play a major role in preventing the deposition of fine particles in the drift (winnowing). It is worth mentioning that the transition from MIS 5e to 5d is depicted by a sharp increase in SS_{mean}, UP10, and coarse EM1, followed by important peaks in the clay % and fine EM3 (Figure 6). As mentioned before, these EMs are related to large and small dust [64], respectively, which are probably transported by vigorous winds over Saharan sources. This is in agreement with [32], who show, in the Alboran record, the occurrence of enhanced aridity and intensified Saharan wind transport during cold D/O periods [23] but well before the coldest SST were attained.

The onset of interstadial MIS 5c is characterized by weak bottom currents (WMDW or deep TDW), pointing to a relatively shallow position of the interface, that are not able to rework the fine sediments (high clay % and very low UP10, Figures 6D and 6E, respectively) mainly defined by EM3 that originate from Ti-rich (high Ti/Ca) SCB dust sources. This situation changes completely by the end of the interstadial, where a sudden increase in UP10, SS_{mean}, silt/clay, and coarse EM1 (Figure 6) may respond to enhanced bottom current speed and a deepening of the interface. This is recorded in the sedimentary facies as a coarsening-up texture from homogeneous mud to mottled mud and then to mottled silt and sandy silt. These strong bottom currents keep working during stadial MIS 5b under cooling and arid conditions in a context of RSL falling [58] (Figure 3) coincident with a very high silt/clay ratio (Figure 6G). Sediments deposited in the drift mainly correspond to the coarse EM1 dust. The fine EM3 is probably affected by winnowing due to flow-speed strengthening, as can be observed by the low values in MS, clay %, and Ti/Ca (Figures 6B, 6D and 6H, respectively). These conditions

are associated with well-ventilated LIW coming from the eastern Mediterranean [81] controlling the sedimentary processes in the DV drift.

The dominant conditions during interstadial MIS 5a likely correspond to that observed in MIS 5c with weak bottom currents that dominate warm periods in a context of an RSL highstand [58] (Figure 3). These conditions would favour a shoaling of the LIW core and, thus, the interface between intermediate and deep water masses. The sluggish bottom currents inferred by the proxies (Figure 6) suggest that during this stage the DV drift is affected by dense currents (deep TDW or WMDW). The sediments deposited in the drift are mainly clay (fine EM3) and silt (EM2) of Ti-bearing composition (high MS and Ti/Ca). Again, as occurred in the offset of MIS 5e and 5c, the enhanced aridity prior to cooling conditions favours the intensification of the Saharan wind transport in relation to the strength of north-westerly winds [32] that deliver coarser particles to the Alboran Sea by the MIS 5a offset. These conditions are depicted by important peaks in UP10, SS_{mean}, silt/clay and coarse EM1 (Figure 6) and defined by the mottled silt and sandy silt facies.

The stadial MIS 4 is characterized by an important RLS lowstand (ca. 90 m below present RSL, [58], Figure 3) that would favour a significant deepening of the interface between intermediate and dense water masses. This coincides with the highest MS recorded in the sediment core that does not correspond to a maximum in EM3 but in EM2, UP10, and Ti/Ca (Figure 6). We argue that this singular record is the result of reworked seamount deposits that feed the contourite system by the action of enhanced bottom currents corresponding to the LIW. Similarly, an increasing followed by a sharp decreasing of the bottom current–speed proxy (SS_{mean}) was also observed by [15] in the Corsica Trough from ca. 80 to 65 kyr. To explain this singular behaviour, these authors proposed a significant deepening of the LIW core (i.e., the vertical position of the maximum flow speed) associated with a significant sea level fall during this time-interval. After the deepening of the LIW core, the settling of both the coarse EM1 and the fine EM3 from aeolian dust occurs in the DV drift since they are no longer transported by this bottom current.

Stadials MIS 3 and MIS 2 are characterized by frequent and sharp fluctuations in $\delta^{18}O$ and SST [30] coupled with millennial-scale variability related to Heinrich Stadials (HS) (Figure 3). Some of these fluctuations are recorded by increasing the paleocurrent strength proxies as peaks in SS_{mean} (HS 5 to 1, see Figure 6F), which are supported by the enhanced deep-water ventilation observed by [9]. The RSL rise [58] by HS 6 implies the shoaling of the LIW core, despite the cold and arid conditions of MIS 3, and deposition of the silty EM2. The anomalous accumulation of carbonate and coarse particles (high UP10 and SS_{mean}, Figures 6E and 6F, respectively) may be related to reworking sediments of the seamount. During MIS 3, the sea-level is reasonably constant with only small RSL fluctuations until the major lowstand (ca. 120 m below present RSL, [58]) occurred in MIS 2 (Figure 3). This may also affect the LIW core position recorded as the UP10 and SS_{mean} variations until the relative increase in both proxies by the HS 2 (Figure 6E,F), resulting from the enhanced LIW speed during the RSL fall [58] just before the abovementioned lowstand. The homogenous and mottled mud facies dominate this period characterized by the silty EM2 and the fine EM3 (high clay %) of the Saharan dust originating from SCB sources (high Ti/Ca and low K/Ti). Some HS are associated with the enhanced wind strength depicted by the deposition of coarse EM1 and UP10 peaks (Figure 6C,E) in the contourite drift record. This is supported by the results of [23], who observed evidence for an increase of northward Saharan dust transport into the Western Mediterranean Sea during HS.

The Younger Dryas (YD) is commonly interpreted as a return towards glacial conditions, with enhanced aridity and an increase in global dust rates [9]. This episode is depicted by high values in bottom current strength (SS_{mean}) as well as important peaks in both coarse EM1 and fine EM3 (Figure 6). The possible descent of the LIW core due to the glacial conditions would push the interface downwards, allowing the LIW to sweep the DV drift during this stage.

During the interglacial MIS 1 (i.e., Holocene), [15] described a drastic reduction of the ventilation and velocity of the LIW, accompanied by a large eustatic sea-level rise. The interface between intermediate and dense water masses is thus located at shallower depths, favouring the DV drift to

be swept by the dense Mediterranean waters (dense TDW and WMDW), as evidenced by a weak activity of the bottom current deduced from the sharp decrease in SS$_{mean}$ and the dominance of the silty EM2 and fine EM3 (Figure 6). The present analysis of CTD profiles (Figure 2) further supports this interpretation. These conditions are similar to those of MIS 5e, with homogeneous mud deposits of K-rich sediments and clay (increasing MS) that probably indicate the SSB sediment source dominance. The low SR and sampling resolution of the cores does not allow further interpretations of the MIS 1 variability.

5. Conclusions

The chronostratigraphic framework indicates that the core K3 spans the last 133 kyr and is one of the oldest piston cores ever retrieved in the Alboran Sea area, except for those of the IODP sites. This allows the identification of the main sediment sources and reconstructing of the paleocurrent variability of Mediterranean intermediate water masses until the Late Pleistocene.

Although in the Alboran Sea region, the main sediment sources are continental runoff from torrential rivers and aeolian dust particles from the Sahara, in the DV drift, only the aeolian supply contributes to the sedimentary record since no evidence of fluvial inputs has been recognized. Three end-members characterize the aeolian particles depending of their grain-size. These are coarse EM1, silty EM2, and fine EM3, characterized by 47, 12, and 3 μm modal sizes, respectively, in which the predominance in the core record is highly dependent on the paleocurrent strength and environmental conditions in the source area. Two main aeolian dust source areas have been recognized in the drift sediments from the Sahara–Sahel Dust Corridor that prevailed during different periods. The possible change between them occurs at approximately the MIS 5-4 transition. At that time, K/Ti displays an important decrease, while Ti/Ca increases significantly, suggesting a change from SSB to SCB sources, with a possible contribution of the Djibouti Ville Seamount deposits. These results point to this area of the Alboran Sea being an excellent sedimentary archive to study the Saharan dust supply to the Mediterranean Sea and the relationships with those records of the North Atlantic African Margin and the trans-Atlantic influence of these airborne particles.

In the DV drift, cold periods are characterized by enhanced bottom current strength—LIW, upper/light TDW—associated with the deepening of the LIW core during sea-level falling and recorded by increasing the winnowing of fine particles, increasing coarse grain-size sediments and decreasing the sedimentation rate. However, during the most pronounced sea-level lowstand in the coldest periods (i.e., the last two glacial maxima), the sedimentation rate is the highest and the sediments are mainly coarse-grained (high silt/clay and UP10). Large increases in the SS$_{mean}$ indicate bottom current acceleration at the end of MIS 6, stadials MIS 5d, 5b, the transition from MIS 5 to 4, as well as the HS occurring during MIS 3 and the YD of MIS 2. Conversely, interglacial periods are characterized by weaker bottom current activity—lower/dense TDW, WMDW—(low SS$_{mean}$ values) mainly related to the shoaling of the LIW core during sea-level rising. This variability is very well correlated with the δ^{18}O record and SST in the Alboran Sea. In the DV drift sediments, the paleocurrent proxies (SS$_{mean}$ and UP10) also record the intensified Saharan wind transport prior to cooling conditions during the enhanced aridity that occurs in the interstadial/stadial transitions.

This study represents a significant contribution to the understanding of paleoclimate changes by means of reconstructing the aeolian dust deposition and paleocurrent variability in the western Mediterranean, as well as the important role of the intermediate Mediterranean waters in palaeoceanographic reconstruction at the millennial scale. These water masses mostly make up the Mediterranean Outflow Water (MOW) that runs along the north-eastern Atlantic Ocean. Therefore, the palaeoceanographic reconstruction presented here may offer new clues to improve the link between the MOW and the Atlantic Meridional Overturning Circulation [84] and thus the climate of the northern hemisphere.

Conflicts of Interest: The authors declare no conflict of interest.

References

1. Stow, D.A.V.; Pudsey, C.J.; Howe, J.A.; Faugères, J.-C.; Viana, A.R. *Deep-Water Contourite Systems: Modern Drifts and Ancient Series, Seismic and Sedimentary Characteristics*; Geological Society London: London, UK, 2002; p. 22.

2. Rebesco, M.; Hernández-Molina, J.; van Rooij, D.; Wåhlin, A. Contourites and associated sediments controlled by deep-water circulation processes: state-of-the-art and future considerations. *Mar. Geol.* **2014**, *352*, 111–154. [CrossRef]

3. McCave, I.N.; Manighetti, B.; Robinson, S.G. Sortable silt and fine sediment size/composition slicing: Parameters for palaeocurrent speed and palaeoceanography. *Paleoceanography* **1995**, *10*, 593–610. [CrossRef]

4. Faugèers, J.-C.; Gonthier, E.; Stow, D.A.V. Contourite drift molded by deep Mediterranean outflow. *Geology* **1984**, *12*, 296. [CrossRef]

5. Bianchi, G.G.; McCave, I.N. Holocene periodicity in North Atlantic climate and deep-ocean flow south of Iceland. *Nature* **1999**, *397*, 515–517. [CrossRef]

6. Birgel, D.; Hass, H. Oceanic and atmospheric variations during the last deglaciation in the Fram Strait (Arctic Ocean): A coupled high-resolution organic-geochemical and sedimentological study. *Quat. Sci. Rev.* **2004**, *23*, 29–47. [CrossRef]

7. Hanebuth, T.J.; Zhang, W.; Hofmann, A.L.; Löwemark, L.A.; Schwenk, T. Oceanic density fronts steering bottom-current induced sedimentation deduced from a 50 ka contourite-drift record and numerical modeling (off NW Spain). *Quat. Sci. Rev.* **2015**, *112*, 207–225. [CrossRef]

8. Lofi, J.; Voelker, A.H.L.; Ducassou, E.; Hernández-Molina, F.J.; Sierro, F.J.; Bahr, A.; Galvani, A.; Lourens, L.J.; Pardo-Igúzquiza, E.; Pezard, P.; et al. Quaternary chronostratigraphic framework and sedimentary processes for the Gulf of Cadiz and Portuguese Contourite Depositional Systems derived from Natural Gamma Ray records. *Mar. Geol.* **2016**, *377*, 40–57. [CrossRef]

9. Cacho, I.; Grimalt, J.O.; Sierro, F.J.; Shackleton, N.; Canals, M. Evidence for enhanced Mediterranean thermohaline circulation during rapid climatic coolings. *Earth Planet. Sci. Lett.* **2000**, *183*, 417–429. [CrossRef]

10. Cacho, I.; Shackleton, N.; Elderfield, H.; Sierro, F.J.; Grimalt, J.O. Glacial rapid variability in deep-water temperature and δ^{18}O from the Western Mediterranean Sea. *Quat. Sci. Rev.* **2006**, *25*, 3294–3311. [CrossRef]

11. Ercilla, G.; Baraza, J.; Alonso, B.; Estrada, F.; Casas, D.; Farrán, M. The Ceuta Drift, Alboran Sea, southwestern Mediterranean. *Geol. Soc. Lond. Memoirs* **2002**, *22*, 155–170. [CrossRef]

12. Sierro, F.J.; Hodell, D.A.; Curtis, J.H.; Flores, J.A.; Reguera, I.; Colmenero-Hidalgo, E.; Barcena, M.A.; Grimalt, J.O.; Cacho, I.; Frigola, J.; et al. Impact of iceberg melting on Mediterranean thermohaline circulation during Heinrich events. *Paleoceanography* **2005**, *20*, PA2019. [CrossRef]

13. Frigola, J.; Moreno, A.; Cacho, I.; Canals, M.; Sierro, F.J.; Flores, J.A.; Grimalt, J.O.; Hodell, D.A.; Curtis, J.H. Holocene climate variability in the western Mediterranean region from a deep water sediment record. *Paleoceanography* **2007**, *22*, 1–16. [CrossRef]

14. Frigola, J.; Moreno, A.; Cacho, I.; Canals, M.; Sierro, F.; Flores, J.; Grimalt, J.; Sierro, F. Evidence of abrupt changes in Western Mediterranean Deep Water circulation during the last 50kyr: A High-Resolution Marine Record from the Balearic Sea. *Quat. Int.* **2008**, *181*, 88–104. [CrossRef]

15. Toucanne, S.; Jouet, G.; Ducassou, E.; Bassetti, M.-A.; Dennielou, B.; Minto'O, C.M.A.; Lahmi, M.; Touyet, N.; Charlier, K.; Lericolais, G.; et al. A 130,000-year record of Levantine Intermediate Water flow variability in the Corsica Trough, western Mediterranean Sea. *Quat. Sci. Rev.* **2012**, *33*, 55–73. [CrossRef]

16. Alonso, B.; López-González, N.; Bozzano, G.; Casas, D.; Ercilla, G.; Juan, C.; Estrada, F.; Garcia, M.; Vázquez, J.T.; Cacho, I.; et al. Djibouti Ville Drift (SW Mediterranean): Sedimentation and record of bottom-current fluctuations during the Pleistocene and Holocene. In Proceedings of the 2nd Deep-Water Circulation Congress, Ghent, Belgium, 10–12 September 2014; pp. 93–94.

17. Martínez-Ruiz, F.; Kastner, M.; Gallego-Torres, D.; Rodrigo-Gámiz, M.R.; Nieto-Moreno, V.; Ortega-Huertas, M. Paleoclimate and paleoceanography over the past 20,000 yr in the Mediterranean Sea Basins as indicated by sediment elemental proxies. *Quat. Sci. Rev.* **2015**, *107*, 25–46. [CrossRef]

18. Ercilla, G.; Juan, C.; Hernández-Molina, F.J.; Bruno, M.; Estrada, F.; Alonso, B.; Casas, D.; Farran, M.; Llave, E.; García, M.; et al. Significance of bottom currents in deep-sea morphodynamics: An example from the Alboran Sea. *Mar. Geol.* **2016**, *378*, 157–170. [CrossRef]

19. Moreno, T.; Querol, X.; Castillo, S.; Alastuey, A.; Cuevas, E.; Herrmann, L.; Mounkaila, M.; Elvira, J.; Gibbons, W. Geochemical variations in aeolian mineral particles from the Sahara–Sahel Dust Corridor. *Chemosphere* **2006**, *65*, 261–270. [CrossRef]

20. Cacho, I.; Grimalt, J.O.; Pelejero, C.; Canals, M.; Sierro, F.J.; Flores, J.A.; Shackleton, N.J. Dansgaard-Oeschger and Heinrich event imprints in Alboran Sea temperatures. *Paleoceanography* **1999**, *14*, 698–705. [CrossRef]

21. Cacho, I.; Grimalt, J.O.; Canals, M.; Sbaffi, L.; Shackleton, N.J.; Schönfeld, J.; Zahn, R. Variability of the western Mediterranean Sea surface temperature during the last 25,000 years and its connection with the Northern Hemisphere climatic changes. *Paleoceanography* **2001**, *16*, 40–52. [CrossRef]

22. Combourieu-Nebout, N.; Turon, J.; Zahn, R.; Capotondi, L.; Londeix, L.; Pahnke, K. Enhanced aridity and atmospheric high-pressure stability over the western Mediterranean during the North Atlantic cold events of the past 50 k.y. *Geology* **2002**, *30*, 863–866. [CrossRef]

23. Moreno, A.; Cacho, I.; Canals, M.; Prins, M.A.; Sánchez-Goñi, M.-F.; Grimalt, J.O.; Weltje, G.J. Saharan Dust Transport and High-Latitude Glacial Climatic Variability: The Alboran Sea Record. *Quat. Res.* **2002**, *58*, 318–328. [CrossRef]

24. Moreno, A.; Cacho, I.; Canals, M.; Grimalt, J.O.; Sanchez-Vidal, A. Millennial-scale variability in the productivity signal from the Alboran Sea record, Western Mediterranean Sea. *Palaeogeogr. Palaeoclim. Palaeoecol.* **2004**, *211*, 205–219. [CrossRef]

25. Bout-Roumazeilles, V.; Combourieu-Nebout, N.; Peyron, O.; Cortijo, E.; Landais, A.; Masson-Delmotte, V. Connection between South Mediterranean climate and North African atmospheric circulation during the last 50,000yrBP North Atlantic cold events. *Quat. Sci. Rev.* **2007**, *26*, 3197–3215. [CrossRef]

26. Jiménez-Espejo, F.J.; Martínez-Ruiz, F.; Rogerson, M.; González Donoso, J.M.; Romero, O.E.; Linares, D.; Sakamoto, T.; Gallego-Torres, D.; Rueda Ruiz, J.L.; Ortega Huertas, M.; et al. Detrital input, productivity fluctuations, and water mass circulation in the westernmost Mediterranean Sea since the Last Glacial Maximum. *Geochem. Geophy. Geosy.* **2008**, *9*, Q11U02. [CrossRef]

27. Nieto-Moreno, V.; Martínez-Ruiz, F.; Giralt, S.; Jiménez-Espejo, F.; Gallego-Torres, D.; Rodrigo-Gámiz, M.; García-Orellana, J.; Ortega-Huertas, M.; De Lange, G.J. Tracking climate variability in the western Mediterranean during the Late Holocene: a multiproxy approach. *Clim. Past Discuss.* **2011**, *7*, 635–675. [CrossRef]

28. Rodrigo-Gámiz, M.; Martínez-Ruiz, F.; Jimenez-Espejo, F.J.; Gallego-Torres, D.; Nieto-Moreno, V.; Romero, O.; Ariztegui, D. Impact of climate variability in the western Mediterranean during the last 20,000 years: Oceanic and atmospheric responses. *Quat. Sci. Rev.* **2011**, *30*, 2018–2034. [CrossRef]

29. De Kaenel, E.; Siesser, W.; Murat, A. Pleistocene calcareous nannofossil biostratigraphy and the western Mediterranean sapropels, Sites 974 to 977 and 979. *Proc. Ocean Drill. Program* **1999**, *161*, 159–183.

30. Martrat, B.; Grimalt, J.O.; López-Martínez, C.; Cacho, I.; Sierro, F.J.; Flores, J.A.; Zahn, R.; Canals, M.; Curtis, J.H.; Hodell, D.A. Abrupt Temperature Changes in the Western Mediterranean over the Past 250,000 Years. *Sciences* **2004**, *306*, 1762–1765. [CrossRef]

31. Matthewson, A.P.; Shimmield, G.B.; Kroon, D.; Fallick, A. A 300 kyr high-resolution aridity record of the North African continent. *Paleoceanograhy* **1995**, *10*, 677–692. [CrossRef]

32. Moreno, A.; Cacho, I.; Canals, M.; Grimalt, J.O.; Sánchez-Goñi, M.F.; Shackleton, N.J.; Sierro, F.J. Links between marine and atmospheric processes oscillating at millennial time-scale. A multy-proxy study of the last 50,000 yr from the Alboran Sea (Western Mediterranean Sea). *Quat. Sci. Rev.* **2005**, *24*, 1623–1636. [CrossRef]

33. Rodriguez-Navarro, C.; Di Lorenzo, F.; Elert, K. Mineralogy and physicochemical features of Saharan dust wet deposited in the Iberian Peninsula during an extreme red rain event. *Atmos. Chem. Phys.* **2018**, *18*, 10089–10122. [CrossRef]

34. Comas, M.C.; García-Dueñas, V.; Jurado, M.J. Neogene tectonic evolution of the Alboran basin from MCS data. *Geo-Mar. Lett.* **1992**, *12*, 157–164. [CrossRef]

35. Maldonado, A.; Campillo, A.C.; Mauffret, A.; Alonso, B.; Woodside, J.; Campos, J. Alboran Sea late cenozoic tectonic and stratigraphic evolution. *Geo-Marine Lett.* **1992**, *12*, 179–186. [CrossRef]

36. Vázquez, J.T.; Vegas, R.; Medialdea, T. Estructuras recientes de deformación en el margen continental del mar de Alborán (Sector Benalmádena-Adra). *Geotemas* **2008**, *10*, 595–598.

37. Palomino, D.; Vázquez, J.-T.; Ercilla, G.; Alonso, B.; López-González, N.; Díaz-Del-Río, V. Interaction between seabed morphology and water masses around the seamounts on the Motril Marginal Plateau (Alboran Sea, Western Mediterranean). *Geo-Marine Lett.* **2011**, *31*, 465–479. [CrossRef]

38. Juan, C.; Ercilla, G.; Estrada, F.; Casas, D.; Alonso, B.; García, M.; Farran, M.; Palomino, D.; Vázquez, J.T.; Llave, E.; et al. Contourite sedimentation in the Alboran Sea: Plio-Quaternary evolution. *Geotemas* **2012**, *13*, 1817–1820.

39. Vázquez, J.T. El margen continental del Mar de Alborán. In *Memoria del Mapa Geomorfológico de España y del Margen Continental a E 1:1.000.000*; Martín Serrano, A., Ed.; IGME: Madrid, Spain, 2005; pp. 189–198.

40. Parrilla, G.; Kinder, T.H.; Preller, R.H. Deep and intermediate mediterranean water in the western Alboran Sea. *Deep. Sea Res. Part A. Oceanogr. Res. Pap.* **1986**, *33*, 55–88. [CrossRef]

41. Millot, C. Circulation in the Western Mediterranean Sea. *J. Mar. Syst.* **1999**, *20*, 423–442. [CrossRef]

42. Gascard, J.; Richez, C. Water masses and circulation in the Western Alboran sea and in the Straits of Gibraltar. *Prog. Oceanogr.* **1985**, *15*, 157–216. [CrossRef]

43. Fabres, J.; Calafat, A.; Sanchez-Vidal, A.; Canals, M.; Heussner, S. Composition and spatio-temporal variability of particle fluxes in the Western Alboran Gyre, Mediterranean Sea. *J. Mar. Syst.* **2002**, *33*, 431–456. [CrossRef]

44. Millot, C. Another description of the Mediterranean Sea outflow. *Prog. Oceanogr.* **2009**, *82*, 101–124. [CrossRef]

45. Millot, C. Heterogeneities of in- and out-flows in the Mediterranean Sea. *Prog. Oceanogr.* **2014**, *120*, 254–278. [CrossRef]

46. Scheuvens, D.; Schütz, L.; Kandler, K.; Ebert, M.; Weinbruch, S. Bulk composition of northern African dust and its source sediments—A compilation. *Earth-Science Rev.* **2013**, *116*, 170–194. [CrossRef]

47. Stuiver, M.; Reimer, P.J. Extended [14]C Data Base and Revised CALIB 3.0 14C Age Calibration Program. *Radiocarbon* **1993**, *35*, 215–230. [CrossRef]

48. Reimer, P.J.; Bard, E.; Bayliss, A.; Beck, J.W.; Blackwell, P.G.; Bronk Ramsey, C.; Buck, C.E.; Cheng, H.; Edwards, R.L.; Friedrich, M.; et al. IntCal13 and Marine13 radiocarbon age calibration curves 0–50,000 years cal BP. *Radiocarbon* **2013**, *55*, 1869–1887. [CrossRef]

49. McCave, I.N.; Bryant, R.J.; Cook, H.F.; Coughanowr, C.A. Evaluation of a laser-diffraction-size analyzer for use with natural sediments. *J. Sediment. Res.* **1986**, *56*, 561–564. [CrossRef]

50. Folk, R.L.; Ward, W.C. Brazos River bar: a study in the significance of grain size parameters. *J. Sediment. Res.* **1957**, *27*, 3–26. [CrossRef]

51. Blott, S.J.; Pye, K. GRADISTAT: A grain size distribution and statistics package for the analysis of unconsolidated sediments. *Earth Surf. Process. Landforms* **2001**, *26*, 1237–1248. [CrossRef]

52. Hall, I.R.; McCave, I.N. Palaeocurrent reconstruction, sediment and thorium focussing on the Iberian margin over the last 140 ka. *Earth Planet. Sci. Lett.* **2000**, *178*, 151–164. [CrossRef]

53. Cisneros, M.; Cacho, I.; Frigola, J.; Sanchez-Vidal, A.; Calafat, A.; Pedrosa-Pàmies, R.; Rumín-Caparrós, A.; Canals, M. Deep-water formation variability in the north-western Mediterranean Sea during the last 2500 yr: A proxy validation with present-day data. *Glob. Planet. Chang.* **2019**, *177*, 56–68. [CrossRef]

54. Dietze, E.; Hartmann, K.; Diekmann, B.; IJmker, J.; Lehmkuhl, F.; Opitz, S.; Stauch, G.; Wünnemann, B.; Borchers, A. An end-member algorithm for deciphering modern detrital processes from lake sediments of Lake Donggi Cona, NE Tibetan Plateau, China. *Sediment. Geol.* **2012**, *243*, 169–180. [CrossRef]

55. Weltje, G.J. End-member modeling of compositional data: Numerical-statistical algorithms for solving the explicit mixing problem. *Math. Geol.* **1997**, *29*, 503–549. [CrossRef]

56. Weltje, G.J.; Tjallingii, R. Calibration of XRF core scanners for quantitative geochemical logging of sediment cores: Theory and application. *Earth Planet. Sci. Lett.* **2008**, *274*, 423–438. [CrossRef]

57. Sánchez-Goñi, M.F.; Harrison, S.P. Millennial-scale climate variability and vegetation changes during the Last Glacial: Concepts and terminology. *Quat. Sci. Rev.* **2010**, *29*, 2823–2827. [CrossRef]

58. Waelbroeck, C.; Labeyrie, L.; Michel, E.; Duplessy, J.; McManus, J.; Lambeck, K.; Balbon, E.; Labracherie, M. Sea-level and deep water temperature changes derived from benthic foraminifera isotopic records. *Quat. Sci. Rev.* **2002**, *21*, 295–305. [CrossRef]

59. Rodrigo-Gámiz, M.; Martínez-Ruiz, F.; Rodríguez-Tovar, F.J.; Jiménez-Espejo, F.J.; Pardo-Igúzquiza, E. Millennial- to centennial-scale climate periodicities and forcing mechanisms in the westernmost Mediterranean for the past 20,000 yr. *Quat. Res.* **2014**, *81*, 78–93. [CrossRef]

60. Ausín, B.; Flores, J.-A.; Sierro, F.-J.; Barcena, M.A.; Hernández-Almeida, I.; Frances, G.; Gutiérrez-Arnillas, E.; Martrat, B.; Grimalt, J.; Cacho, I.; et al. Coccolithophore productivity and surface water dynamics in the Alboran Sea during the last 25kyr. *Palaeogeogr. Palaeoclim. Palaeoecol.* **2015**, *418*, 126–140. [CrossRef]

61. Weltje, G.J.; Prins, M.A. Genetically meaningful decomposition of grain-size distributions. *Sediment. Geol.* **2007**, *202*, 409–424. [CrossRef]

62. Hodell, D.; Crowhurst, S.; Skinner, L.; Tzedakis, P.C.; Margari, V.; Channell, J.E.T.; Kamenov, G.; Maclachlan, S.; Rothwell, G. Response of Iberian Margin sediments to orbital and suborbital forcing over the past 420 ka. *Paleoceanograhy* **2013**, *28*, 185–199. [CrossRef]

63. Hodell, D.A.; Evans, H.F.; Channell, J.E.; Curtis, J.H. Phase relationships of North Atlantic ice-rafted debris and surface-deep climate proxies during the last glacial period. *Quat. Sci. Rev.* **2010**, *29*, 3875–3886. [CrossRef]

64. Evans, R.D.; Jefferson, I.F.; Kumar, R.; O'Hara-Dhand, K.; Smalley, I.J. The nature and early history of airbone dust from North Africa; in particular the Lake Chad basin. *J. Afr. Earth Sci.* **2004**, *39*, 81–87. [CrossRef]

65. Livingstone, I.; Warren, A. *Aeolian Geomorphology: An Introduction*; Longman Pub Group: Harlow, UK, 1996; p. 211.

66. Rothwell, R.G.; Croudace, I.W. Twenty Years of XRF Core Scanning Marine Sediments: What Do Geochemical Proxies Tell Us. In *Micro-XRF Studies of Sediment Cores: Applications of A Non-Destructive Tool for the Environmental Sciences*, 1st ed.; Croudace, I.W., Rothwell, R.G., Eds.; Springer: Dordrecht, The Netherlands, 2015; pp. 25–102.

67. Calvert, S.E.; Pedersen, T.F. Elemental Proxies for Palaeoclimatic and Palaeoceanographic Variability in Marine Sediments: Interpretation and Application. In *Proxies in Late Cenozoic Paleoceanography*, 1st ed.; Hillaire-Marcel, C., De Vernal, A., Eds.; Elsevier: Amsterdam, The Netherlands, 2007; Volume 1, pp. 567–644.

68. Hanebuth, T.J.; Lantzsch, H. A Late Quaternary sedimentary shelf system under hyperarid conditions: Unravelling climatic, oceanographic and sea-level controls (Golfe d'Arguin, Mauritania, NW Africa). *Mar. Geol.* **2008**, *256*, 77–89. [CrossRef]

69. Giermann, G.; Pfannenstiel, M.; Wimmenauer, W. Relations entre morphologie, tectonique et volcanisme en mer d'Alboran (Mediterranée Occidentale). *Compt. Rend. Somm. Soc. Fr.* **1968**, *4*, 116–118.

70. Kenyon, N.H.; Ivanov, M.K.; Akhmetzhanov, A.M.; Akhmanov, G.G. Multidisciplinary Study of Geological Processes on the North East Atlantic and Western Mediterranean Margins IOC Technical Series No. 56, UNESCO. 2000. Available online: https://folk.uio.no/adrianom/TTR%20WWW/TTR/cruises/ttr9.html (accessed on 3 June 2019).

71. Hoernle, K.; Bogaard, P.V.D.; Duggen, S.; Mocek, B.; Garbe-Schönberg, D. Evidence for Miocene subduction beneath the Alboran Sea: 40Ar/39 Ar dating and geochemistry of volcanic rocks from Holes 977A and 978A. *Proc. Ocean Drill. Program* **1999**, *161*, 357–373.

72. Henrich, R.; Cherubini, Y.; Meggers, H. Climate and sea level induced turbidite activity in a canyon system offshore the hyperarid Western Sahara (Mauritania): The Timiris Canyon. *Mar. Geol.* **2010**, *275*, 178–198. [CrossRef]

73. Caquineau, S.; Gaudichet, A.; Gomes, L.; Magonthier, M.-C.; Chatenet, B. Saharan dust: Clay ratio as a relevant tracer to assess the origin of soil-derived aerosols. *Geophys. Res. Lett.* **1998**, *25*, 983–986. [CrossRef]

74. Hernández-Molina, F.J.; Larter, R.D.; Rebesco, M.; Maldonado, A. Miocene reversal of bottom water flow along the Pacific Margin of the Antarctic Peninsula: Stratigraphic evidence from a contourite sedimentary tail. *Mar. Geol.* **2006**, *228*, 93–116. [CrossRef]

75. Rodrigo, F.S.; Pozo-Vazquez, D.; Esteban-Parra, M.J.; Castro-Diez, Y. A reconstruction of the winter North Atlantic Oscillation index back to A.D. 1501 using documentary data in southern Spain. *J. Geophys. Res. Space Phys.* **2001**, *106*, 14805–14818. [CrossRef]

76. Sánchez-Goñi, M.F.; Cacho, I.; Turon, J.L.; Guiot, J.; Sierro, F.J.; Peypouquet, J.P.; Grimalt, J.O.; Schackleton, N.J. Synchroneity between marine and terrestrial responses to millennial scale climatic variability during the last glacial period in the Mediterranean region. *Clim. Dyn.* **2002**, *19*, 95–105.

77. Ercilla, G.; Juan, C.; Periáñez, R.; Alonso, B.; Abril, J.M.; Estrada, F.; Casas, D.; Vázquez, J.T.; D'Acremont, E.; Gorini, C.; et al. Influence of alongslope processes on modern turbidite systems and canyons in the Alboran Sea (southwestern Mediterranean). *Deep. Sea Res. Part I: Oceanogr. Res. Pap.* **2019**, *144*, 1–16. [CrossRef]

78. Rossignol-Strick, M. Mediterranean Quaternary sapropels, an immediate response of the African monsoon to variation of insolation. *Palaeogeogr. Palaeoclim. Palaeoecol.* **1985**, *49*, 237–263. [CrossRef]

79. Stow, D.A.V.; Faugères, J.C. Contourite facies and the facies model. In *Contourites*; Rebesco, M., Camerlenghi, A., Eds.; Elsevier: Amsterdam, The Netherlands, 2008; pp. 223–256.

80. Nolet, G.J.; Corliss, B.H. Benthic foraminiferal evidence for reduced deep-water circulation during sapropel deposition in the eastern Mediterranean. *Mar. Geol.* **1990**, *94*, 109–130. [CrossRef]

81. Myers, P.G. Flux-forced simulations of the paleocirculation of the Mediterranean. *Paleoceanography* **2002**, *17*, 9-1. [CrossRef]

82. Rossignol-Strick, M. African monsoons, an immediate climate response to orbital insolation. *Nature* **1983**, *304*, 46–49. [CrossRef]

83. Roether, W.; Klein, B.; Beitzel, V.; Manca, B.B. Property distributions and transient-tracer ages in Levantine Intermediate Water in the Eastern Mediterranean. *J. Mar. Syst.* **1998**, *18*, 71–87. [CrossRef]

84. Bartoli, G.; Sarnthein, M.; Weinelt, M.; Erlenkeuser, H.; Garbe-Schönberg, D.; Lea, D. Final closure of Panama and the onset of northern hemisphere glaciation. *Earth Planet. Sci. Lett.* **2005**, *237*, 33–44. [CrossRef]